Journal of Crystal Growth 542 (2020) 125609

Contents lists available at ScienceDirect

Journal of Crystal Growth

journal homepage: www.elsevier.com/locate/jcrysgro

Chemical vapor transport synthesis, characterization and compositional tuning of ZrS_xSe_{2-x} for optoelectronic applications

Joshua J. Fox[a,*], Saiphaneendra Bachu[b], Randal L. Cavalero[a], Robert M. Lavelle[a], Sean M. Oliver[c], Sam Yee[c], Patrick M. Vora[c], Nasim Alem[b], David W. Snyder[a,d]

[a] *Electronic Materials and Devices Department, Applied Research Laboratory, Pennsylvania State University, University Park, PA 16802, USA*
[b] *Department of Materials Science and Engineering, The Pennsylvania State University, University Park, PA 16802, USA*
[c] *Quantum Materials Center, George Mason University, Fairfax, VA 22030, USA*
[d] *2-Dimensional Crystal Consortium, Materials Research Institute, Pennsylvania State University, University Park, PA 16802, USA*

ARTICLE INFO

Communicated by R. Bhat

Keywords:
A1. Composition tuning
A1. Bandgap engineering
B1. 2D materials
B1. Transition metal dichalcogenides
B1. TMD alloy

ABSTRACT

ZrS_2, $ZrSe_2$ and mixed alloy ZrS_xSe_{2-x} materials were achieved through chemical vapor transport. The incongruent melting system of Zr-S-Se formed crystalline layered flakes as a transport product that grew up to 2 cm in lateral size with cm-scale flakes consistently obtained for the entire compositional range exhibiting visible hexagonal features. Bulk flakes of the series ZrS_xSe_{2-x} ($x = 0$, 0.15, 0.3, 0.6, 1.05, 1.14, 1.51, 1.8 and 2) were analyzed through Raman spectroscopy revealing significant convolution of primary bonding modes and shifting of Raman features as a function of increasing sulfur composition. Additionally, activation of new modes not present in the pure compounds are observed as effects which result from disorder introduced into the crystal due to the random mixing of S-Se in the alloying process. Further structural characterization was performed via x-ray diffraction (XRD) on the layered flakes to evaluate the progression of layer spacing function of alloy composition which was found to range between 6.24 Å for $ZrSe_2$ and 5.85 Å for ZrS_2. Estimation of the compositional ratios of the alloy flakes through energy dispersive spectroscopy (EDS) large-area mapping verified the relation of the targeted source stoichiometry represented in the layered flakes. Atomic-resolution high angle annular dark field (HAADF)-scanning transmission electron microscopy (STEM) imaging was performed on the representative $Zr(S_{0.5}Se_{0.5})_2$ alloy to validate the 1T atomic structure and observe the arrangement of the chalcogenide columns stacks. Additionally, selected area diffraction pattern generated from the [0 0 0 1] zone axis revealed the in-plane lattice parameter to be approximately 3.715 Å.

1. Introduction

The discovery of graphene has triggered increasing focus on graphene-like layered materials which possess band gap properties suitable for semiconductor applications. ZrS_2 and $ZrSe_2$ as indirect-semiconductor transition metal dichalcogenides (TMDs) offer promising characteristics as active elements in optoelectronics based on high anisotropy of the 1T layered structure [1–3]. In this structure, ZrS_2 and $ZrSe_2$ exhibit strong, mixed covalent/ionic bonding character within the layer promoting excellent conduction properties through the layer sheet. This structural anisotropy provides opportunities for large-area excitation by photon absorption for optically active devices, such as photovoltaics, if scalable synthesis methods for high quality single crystals and thin films can be developed.

To date, ZrS_2 and $ZrSe_2$ have been evaluated as promising candidates for optoelectronic applications through theoretical and experimental studies [4–6] indicating the band gap energies should range from 1.2 eV for $ZrSe_2$ toward 1.8 eV for ZrS_2. In addition, it has been predicted that uniaxial strain applied to ZrS_2 sheets may alter the band structure in a way that induces a transition from indirect to direct band gap semiconductor [7]. There are rich possibilities to further explore the ZrS_2-$ZrSe_2$ system by considering the ZrS_xSe_{2-x} mixed alloy system, providing an opportunity for highly customizable and tailorable device structure with expanded material choices and spatial property variations. ZrS_xSe_{2-x} ternary alloy single crystal flakes have previously been synthesized through the chemical vapor transport (CVT) method [8–11] showing that the band gap progresses as approximately a linear function with composition and confirming modifiable optical absorption characteristics in the visible spectrum attributed to differences in bonding of randomly-mixed chalcogenide constituents and their

---

[*] Corresponding author at: 183 The 230 Building, 230 Innovation Blvd, University Park, PA 16802, USA.
E-mail address: Jjf5345@arl.psu.edu (J.J. Fox).

https://doi.org/10.1016/j.jcrysgro.2020.125609
Received 14 October 2019; Received in revised form 13 March 2020; Accepted 16 March 2020

electronegativity difference within the layered structure. An additional possibility exists to evaluate the band gap and optical absorption evolution of mixed ZrS_xSe_{2-x} alloys with application of strain which merits further investigation.

In order to further study the growth behavior and composition-property assessments, the CVT method has been employed here to produce ZrS_xSe_{2-x} layered crystal flakes over a wide compositional range with source stoichiometry of $x = 0, 0.2, 0.5, 0.8, 1.0, 1.2, 1.5, 1.8, 2.0$ as nominal values. The source stoichiometry has been found to match reasonably well with compositional determinations of CVT-grown flakes through energy dispersive spectroscopy (EDS) area mapping, confirming a uniform mixing distribution of chalcogenide members along with the presence of Hf as a metal source constituent that must be considered in source material selection for synthesis of Zr-based TMDs. The Raman signatures of select ZrS_xSe_{2-x} alloys were also collected to illustrate the activation of alloy-specific vibrational modes along with shifting and broadening of binary endmember Raman features with changing composition. The oriented flakes were also scanned with x-ray diffraction (XRD) which provides a progression of the interlayer spacing character as a function of composition. An additional component of this study includes a preliminary examination of the atomic-scale arrangements of the chalcogenide atoms surrounding the Zr metal atoms for a mixed alloy $Zr(S_{0.5}Se_{0.5})_2$ system to validate the expected structural formation, crystalline quality and homogenous chalcogenide mixing in the flakes.

2. Materials and methods

The growth of ZrS_xSe_{2-x} alloys was performed through the chemical vapor transport method. Growth trials were conducted in a four-zone tube furnace that was fitted with a ceramic center baffle that produced an appropriate temperature gradient (see Fig. 1). A standard heating procedure was utilized for the furnace which involved several key stages. Initially the furnace was heated slowly at 0.50 °C/min from room temperature to an intermediate temperature of 450 °C and maintained equally across each heating zone for 24 h in order to initiate an equilibrium of sulfur vapor sublimation and allow for metal-chalcogenide pre-reactions and source compounding to occur. Following this stage, the furnace temperature was ramped upward at a rate of 0.70 °C/min and 0.60 °C/min to reach reaction zone temperature of 900 °C and growth zone temperature of 800 °C respectively. The temperature gradient was found to maximize the transport product density and enhance the size of the flakes that were produced. The gradient was held constant for 200 h following a slow cooling at 0.15 °C/min back to room temperature.

Source materials were loaded into a quartz ampoule with inner diameter of 10 mm with 2 mm wall thickness. The ampoules were also loaded with an iodine transport agent at a concentration of 5 mg/cm^3. The ampoules were evacuated at a turbo pumping station to a pressure of approximately 10^{-5} Torr and sealed with oxy-hydrogen torch to a total length of 180 mm. Two Zr sources were employed to observe any potential differences in the mass transport and/or formation of growth product. Each source stoichiometry used the two Zr source materials, one of which being a fine grain −325 mesh powder (Sigma-Aldrich, Product #756385-5G 99.5% metals basis, excluding Hf) and the other being a bulk 3–6 mm Zr lump source (Alfa Aesar, Product #36253 99.8% metals basis, excluding Hf) combined with chalcogenide sources comprising selenium powder (Alfa Aesar, Product #036208, −200 mesh 99.999% metals basis) and sulfur pieces (Alfa Aesar, Product #10755, Puratronic® 99.999% metals basis). One will note the presence of Hf contained within the two Zr sources as a natural impurity that cannot be refined beyond the purification process absent of extensive effort and monetary expense. The Hf content in the lot of Zr powder utilized in the growths was provided as 1.8 atomic %. Likewise, the Zr lump source Hf content was provided as 1.4 atomic %. Therefore, one may expect the presence of Hf at a considerable level beyond a moderate or high-doping concentration as an impurity constituent in the ZrS_xSe_{2-x} flakes grown.

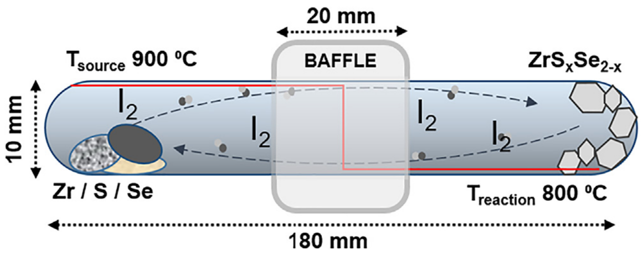

Fig. 1. Chemical Vapor Transport process ampoule schematic showing orientation of source and reaction zones and respective temperatures divided by refractory baffle to provide temperature gradient.

Optical characterization was performed using the Amscope Circuit Zoom Stereo Microscope with 144 LED white light ring. The compositional ratios of the grown flakes were determined through EDS with large-area imaging and compositional mapping performed with FEI Nova NanoSEM 630 SEM with field emission excitation source equipped with Bruker QUANTAX EDS detector for alloy compositional estimates. Further stoichiometry quantification was achieved by inductively coupled plasma mass spectroscopy (ICP-MS) performed by EAG Laboratories. Raman measurements were carried out at room temperature on the Horiba LabRam instrument using a 532 nm excitation source operating a 0.41 mW. The x-ray diffraction spectra were obtained utilizing a Malvern Panalytical Empryean X-Ray diffractometer using Cu K-alpha radiation source and PEXcel 3D detector operating in reflection mode with a theta-theta goniometer.

Preliminary transmission electron microscopy (TEM) characterization was performed on the $Zr(S_{0.5}Se_{0.5})_2$ ($x = 1$) alloy to determine the crystalline quality and chalcogen distribution in the lattice. Samples for TEM characterization were prepared using mechanical exfoliation of CVT grown flakes onto Si/SiO_2 wafers [12] followed by a gentle polycarbonate (PC)/polydimethylsiloxane (PDMS) based transfer of exfoliated flakes onto TEM grids [13]. Mechanical exfoliation was carried out inside a glove box to minimize the exposure of exfoliated crystals to ambient atmosphere. This proved to improve the quality of imaging because Zr based dichalcogenides are known to be sensitive to outside environment. Also, the transfer method that was chosen for this study minimizes the time spent by the exfoliated crystals outside the glove box and exposure to harsh chemicals before going into a TEM for characterization. Briefly, the transfer process begins with coating the Si/SiO_2 wafer, onto which flakes were exfoliated, with a solution of PC in chloroform (∼0.04 g in 0.8 mL) to form a thin PC film on the surface. Then, a PDMS stamp was used to detach the PC film along with the exfoliated flakes from the wafer. The "PDMS/PC/$Zr(S_{0.5}Se_{0.5})_2$ flakes" assembly is then turned upside down so the $Zr(S_{0.5}Se_{0.5})_2$ flakes are on top and PDMS is on bottom. A Quantifoil holey carbon Cu TEM grid is placed on the top of the exfoliated flakes with the carbon side of the grid facing the flakes. A drop of isopropanol (IPA) is dropped on the top to separate the "$Zr(S_{0.5}Se_{0.5})_2$ flakes/PC" assembly from the PDMS. At this point, "TEM grid/$Zr(S_{0.5}Se_{0.5})_2$ flakes/PC" assembly floats on top of PDMS which can be captured with a pair of tweezers. The assembly is then kept on a hot plate at 120 °C to let the IPA dry so the PC film is adhered to the carbon film on the TEM grid. PC is dissolved from the assembly using a chloroform bath in the final step of the transfer to leave the TEM grid with just the exfoliated flakes.

FEI Tecnai G2 20 XTWIN TEM was used to obtain selected area diffraction patterns (SADP) which are then used to determine the symmetry and in-plane lattice parameters of the alloy. Atomic-resolution high angle annular dark field (HAADF)-scanning transmission electron microscopy (STEM) imaging was performed using double aberration corrected FEI Tian^3 G2 microscope operated at 80 kV to assess atomic structure to reveal the chalcogen distribution. HAADF-

(a) Zirconium Lump Source

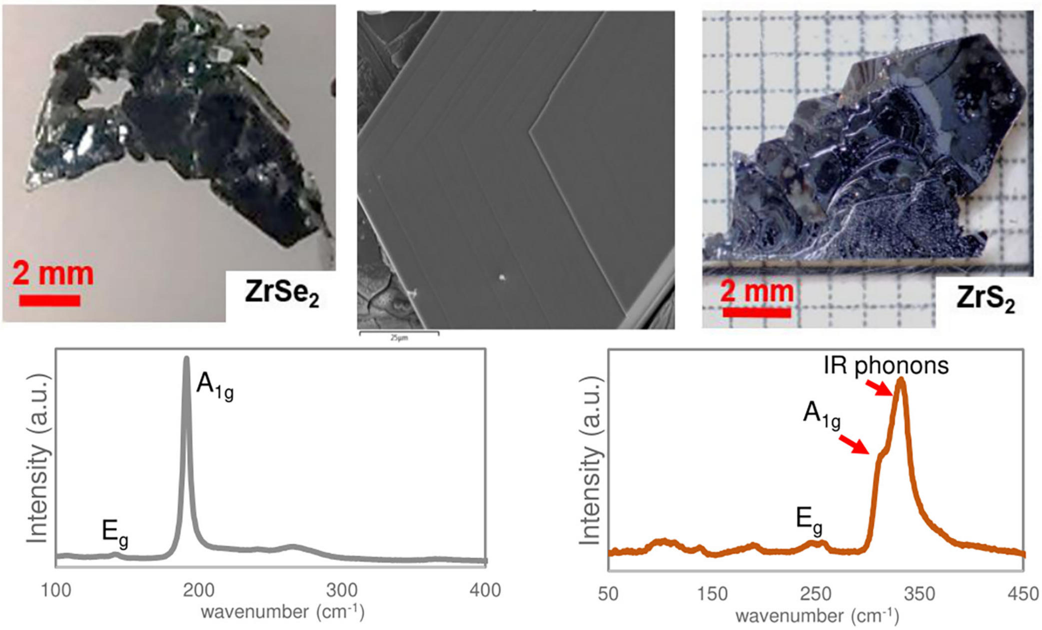

(b) Zirconium Lump Source

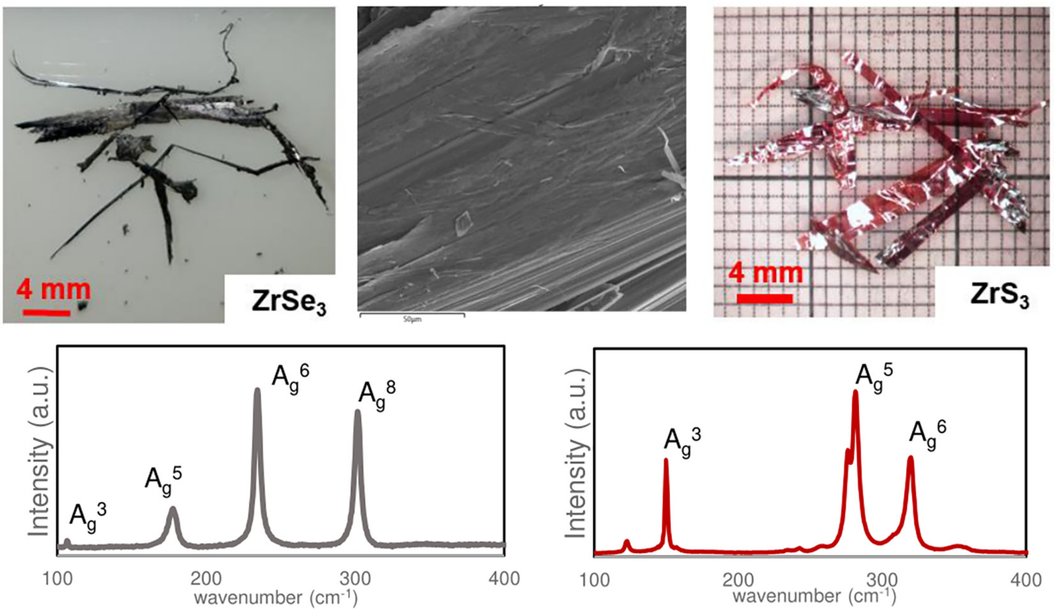

Fig. 2. Optical images of CVT flake products as a function of zirconium metal source with representative Raman spectra for (a) ZrS_2 and $ZrSe_2$ materials as a function of 3–6 mm Zr lump source and (b) ZrS_3 and $ZrSe_3$ materials grown by the −325 mesh Zr powder source.

STEM imaging was performed using 30 mrad semi convergence angle and 60 pA current.

3. Results and discussion

The ZrS_xSe_{2-x} flakes grown in this study exhibited a sharp contrast in structure and stoichiometry as a function of the zirconium source selected to carry out the CVT process. The morphology of the flakes display large-scale hexagonal features with lateral size up to approximately 20 mm which could be reliably obtained for all compositions when utilizing the Zr lump source particles. However, the reaction products of experiments using the −325 mesh Zr powder source exhibit a needle-like morphology indicating a linear or chain-type of growth morphology which is more revealing of a ZrX_3-type structure. The morphology contrast for binary components $ZrSe_2$ and ZrS_2 is displayed in Fig. 2 with optical magnified images and SEM micrographs.

The structure and flake size are representative to the type of reaction products that were obtained for growth of ZrS_xSe_{2-x} mixed alloys. In addition to the visual structural differences, the Raman signatures varied of materials obtained as a function of source choice which is displayed as well in Fig. 2. Through this we have observed that the products obtained by using the −325 mesh Zr source are a predominant chalcogenide-rich phase indicating a ZrS_xSe_{3-x} stoichiometry in the flakes while the Zr lump source allowed for growth of the desired dichalcogenide phase ZrS_xSe_{2-x} single crystals as confirmed by Raman spectra of the binary materials and EDS compositional ratios displayed for mixed alloy in Fig. 3. The lateral sizes and morphology of the flakes from this study closely resemble the visual characteristics of ZrS_xSe_{2-x}

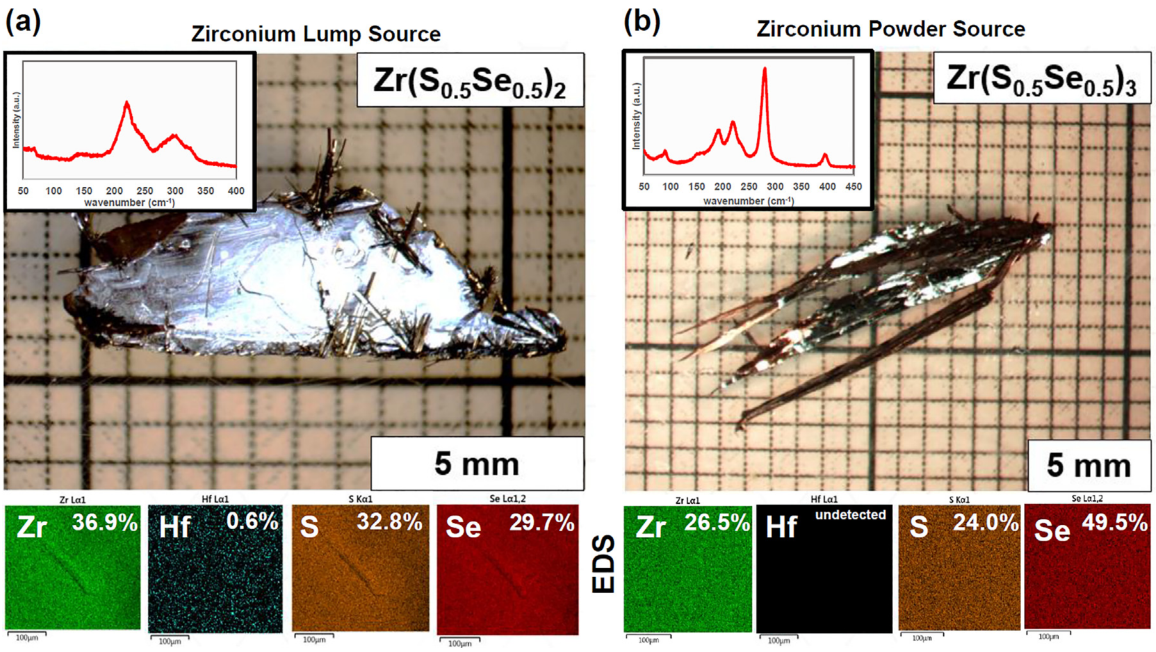

Fig. 3. Optical images of CVT flake products as a function of zirconium metal source with EDS compositional area maps and inserts of the respective Raman spectra as a function of (a) 3–6 mm Zr lump source and (b) −325 mesh Zr powder source.

and ZrS_xSe_{3-x} materials discussed in prior growth studies [8,10].

The large area EDS elemental mapping shown in Fig. 3 represents the mixed alloy growth behavior of the crystalline flakes produced as a function of zirconium source material. For all compositions it is apparent that the mixing of S and Se is homogenous across large areas indicating uniformity of S and Se distribution within the bulk flakes. An interesting observation is the presence of Hf that was measured through EDS as at significant impurity presence within ZrS_xSe_{2-x} flakes. It is also noted that Hf was not detected in any ZrS_xSe_{3-x} materials by EDS indicating a remarkably lower Hf content in the ZrS_xSe_{3-x} flakes. The service of inductively coupled plasma mass spectroscopy (ICP-MS) was sought (EAG Laboratories) to perform sensitive quantification of the metals impurity presence and stoichiometric ratio of Zr:Hf within each type of flake grown as a function of zirconium source. The values displayed in Table 1 reveal Hf is indeed present likewise in the ZrS_xSe_{3-x} material though on the order of approximately one magnitude lower than that measured in the ZrS_xSe_{2-x} flakes. This may suggest that Hf is not as well accommodated by the ZrS_xSe_{3-x} chain-like structure and may contribute to added defect density and stacking faults/irregularities of the bulk flakes. The ICP-MS quantifications also further confirm the structural contrast between each type of flake obtained as the chalcogen:metal ratio is found to be approximately 2 for the ZrS_xSe_{2-x} formed from Zr lump source and close to 3 for the ZrS_xSe_{3-x} material formed by −325 mesh Zr source powders respectively. The Hf impurity level from each vendor was specified to by 1.8% for 3–6 mm Zr lump source and 1.4% for −325 mesh Zr powder so with a similarity in the Hf content in each source this cannot be attributed to the difference in Hf levels measured in the CVT flake products. Instead, we consider the source particle morphology to be the primary attributing factor as a particle with a high surface-volume ratio may contain a greater presence of oxidation shells on particle outer surfaces which can hinder the Zr sublimation and transport during the CVT process. This effect is magnified in the Zr powder source to a higher degree relative to the larger gain lump source where the surface-to-volume ratio is approximately 2 orders of magnitude lower. The results suggest a lower transport rate of Zr in the experiments using the Zr fine grain powder, which results in a metal-deficient vapor species at the reaction zone promoting formation of a chalcogenide-rich layered phase. Further investigation will be needed to explicitly confirm this source effect of metal sublimation and mass transport rates as a function of oxide presence, thickness and particle morphology, however this factor should be considered in experimental design of TMD bulk single crystal CVT processes.

Table 1
ICP-MS molar quantification of metals content in the as-grown $Zr(S_{0.5}Se_{0.5})_2$ and $Zr(S_{0.5}Se_{0.5})_3$ flakes as a function of Zr source selection with the ratio of chalcogenide to metal stoichiometry.

Zr Source	Composition	Zr	Hf	Chalcogenide:Metal
3–6 mm lump	$Zr(S_{0.5}Se_{0.5})_2$	31.6	0.4	2.1
−325 mesh powder	$Zr(S_{0.5}Se_{0.5})_3$	22.3	0.07	3.4

As indicated in Fig. 3, the targeted stoichiometry of equivalent S and Se content in the mixed alloy flakes is represented. The chalcogen compositional estimations made through EDS elemental mapping reveals the stoichiometric S:Se ratio matches well with the source stoichiometry loaded into the ampoule for the ZrS_xSe_{2-x} flakes. In the ZrS_xSe_{3-x} there appears to be a higher variation in chalcogenide content with respect to the source stoichiometry which suggests some added molar compensation may be needed in experimental design for synthesis of ZrS_xSe_{3-x} by similar vapor reaction and transport growth methods. A tabular listing of atomic content in ZrS_xSe_{2-x} flakes for all compositions determined through EDS growth by Zr lump source is given in Table 2.

Raman spectra were obtained at room temperature to elucidate the effects of the alloying process on the vibrational modes in ZrS_xSe_{2-x} flakes. The 1T crystal structure of the endpoint compounds $ZrSe_2$ ($x = 0$) and ZrS_2 ($x = 2$) belongs to the D_{3d} point group (space group $P\bar{3}m1$, #164). Therefore, the Raman-active modes have A_{1g} and E_g symmetry. A_{1g} and E_g modes correspond to either out-of-plane or in-plane vibrations of the chalcogen atoms, respectively, while the transition metal atoms remain stationary. As shown in the Raman spectra of Fig. 4, we measure the E_g and A_{1g} modes in $ZrSe_2$ at ~147 cm^{-1} and ~194 cm^{-1} and in ZrS_2 at ~251 cm^{-1} and ~320 cm^{-1}, respectively, which agree well with previous Raman measurements. The large peak at ~334 cm^{-1} is believed to result from hybridization of the Raman-active A_{1g} mode with infrared-active modes [14].

Measurements displayed in Fig. 4 reveal a smooth evolution of the

Table 2
Alloy EDS determinations considering instrumental measurement errors.

Alloy	Source Stoichiometry Parameter (x)	Zr Atomic % (± 0.10%)	Hf Atomic % (± 0.01%)	S Atomic % (± 0.57%)	Se Atomic % (± 0.50%)	Calculated EDS Composition Parameter
$Zr(S_{0.1}Se_{0.9})_2$	0.2	33.7	0.48	5.0	60.8	**0.151**
$Zr(S_{0.25}Se_{0.75})_2$	0.5	34.0	1.36	9.50	55.1	**0.294**
$Zr(S_{0.4}Se_{0.6})_2$	0.8	35.3	0.54	19.5	44.6	**0.609**
$Zr(S_{0.5}Se_{0.5})_2$	1.0	35.8	0.69	30.9	32.7	**0.970**
$Zr(S_{0.6}Se_{0.4})_2$	1.2	36.2	0.59	36.0	27.2	**1.14**
$Zr(S_{0.75}Se_{0.25})_2$	1.5	37.0	0.53	47.3	15.2	**1.51**
$Zr(S_{0.9}Se_{0.1})_2$	1.8	40.2	0.41	53.2	6.2	**1.79**

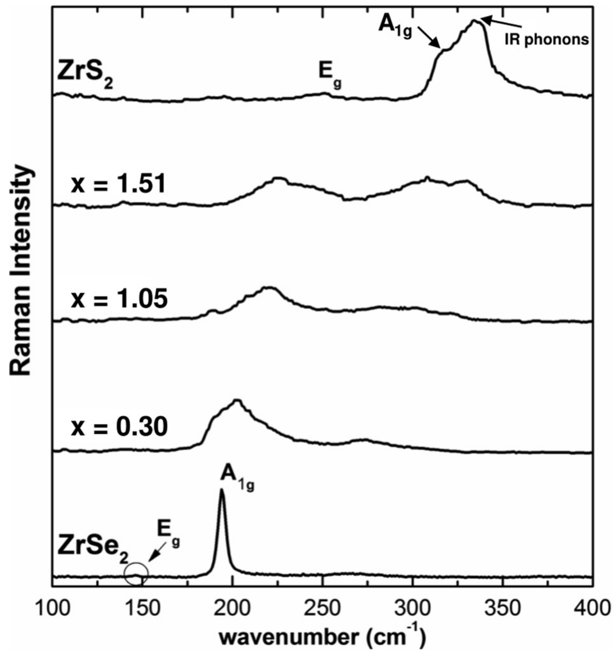

Fig. 4. Raman spectra of ZrS_xSe_{2-x} alloys (x = 0.30, 1.05, 1.51) and ZrS_2, $ZrSe_2$ binary endpoints at room temperature.

Raman spectra as $ZrSe_2$ and ZrS_2 are alloyed together. The alloys show a superposition of the features from the endpoint compounds, as seen in previous studies of TMD alloys [15], but with significant asymmetrical broadening and decreased intensity. Asymmetrical broadening of the vibrational modes is known to result from relaxation of the $\vec{q} = 0$ Raman selection rules due to broken translational symmetry in the lattice [16]. Here, broken translational symmetry is caused by substitutional atoms incorporated into the lattice during the alloying process, and scattering off of these disorder sites results in the activation of finite momentum phonons, as seen in the TMD alloys $Mo_{1-x}W_xTe_2$ [17], as well as other alloy systems such as $Al_xGa_{1-x}N$ [18] and $Ga_{1-x}Al_xAs$ [16]. Additional features present only in the alloys are most likely the result of disorder-enhanced infrared modes or new modes originating from different S-Se arrangements around the Zr atoms that yield spatial force constant variations that influence lattice dynamics [17,19,20]. A more detailed discussion of these Raman features is presented in Ref. [21].

X-ray diffraction was also performed as a measure to illustrate the compositional shift of the ZrS_xSe_{2-x} crystals by orienting the flakes as flat samples to be scanned in 2-theta range of 10–70 degrees where the reflections of the oriented (0 0 *l*) peaks for *l* = 1, 2, 3, 4 were found. With increasing S content, thus reducing the content of the larger Se constituents, there is a shift in peak position for each of these reflections toward higher 2-theta values as an indication of decreasing plane spacing. Fig. 5 shows the shifting of these reflections for each composition and a plot of *c*-plane spacing.

The ZrS_xSe_{2-x} flakes as grown in this study reveal the *c*-parameter ranges from 5.851 Å for ZrS_2 increasing to 6.242 Å for $ZrSe_2$. The values of several ZrS_xSe_{2-x} compositions are given in Table 3 and compared to values of equivalent composition provided by earlier works of ZrS_xSe_{2-x} alloys grown through CVT processes. The functions of the *c*-parameter for each study confirms the quadratic evolution of the c-plane spacing which diminishes as a function of increasing sulfur content.

It is noted that the values recorded for ZrS_xSe_{2-x} materials in the present study are consistently above what has been reported in the prior works. This is directly attributed to the significant Hf content in the crystals as an impurity constituent as outlined previously. The substitution of a higher period transition metal provides an enlargement effect of the *c*-parameter without perturbing the hexagonal layered structure shared by TMD materials. This effect resembles the lattice parameter evolution determined experimentally through XRD in an earlier assessment and structural characterization of CVT-prepared $Mo_{1-x}W_xSe_2$ alloy single crystals [22].

Further, the $Zr(S_{0.5}Se_{0.5})_2$ (x = 1) alloy was examined using transmission electron microscopy (TEM) to understand the atomic structure of the CVT-grown crystal at atomic length scale to visualize the defects present in the material, such as Hf impurities, and observe distribution of chalcogens (S/Se) atoms in the lattice. Additionally, TEM characterization was used to measure the in-plane lattice parameters and to confirm the 1T stacking expected from the crystal structure of Zr based dichalcogenides.

Fig. 6(a) is an image of an exfoliated flake transferred to Quantifoil holey carbon TEM grid using the transfer method described in the Materials and Methods section. Selected area diffraction pattern (SADP) obtained from the flake is presented in Fig. 6(b). The spots in the SADP highlight the single crystal nature and hexagonal symmetry of the crystal. The spots were utilized to calculate the interplanar spacing values of the indexed planes which in turn were used to deduce the in-plane lattice parameters of the crystal. Lattice parameter values obtained from the three primary reflections indicated in the SADP are 3.707 Å, 3.719 Å, 3.710 Å. The values are well-aligned to the values previously reported for the $Zr(S_{0.5}Se_{0.5})_2$ (x = 1) alloy (~3.715 Å) [23,24], thus confirming the nominal composition of the alloy obtained from EDS and ICP-MS measurements. The zone axis of SADP is [0 0 0 1]. Atomic-resolution HAADF-STEM imaging further revealed the atomic arrangement in the sample, as shown in Fig. 6(c). Since HAADF-STEM images are dominated by atomic number (z) contrast, Zr metal atoms (z = 40) appear brighter compared to chalcogen atoms (z of sulfur = 16; z of selenium = 34). A closer inspection reveals some of the metal atoms are brighter than other metal atoms in the lattice. They are highlighted by dashed yellow circles and are attributed to Hf impurities in the crystal because Hf atoms (z = 72) have higher atomic number compared to Zr atoms. A higher magnification image was used for more in-depth analysis of the atomic structure as explained in Fig. 6(d)–(f). First, Fig. 6(d) underlines the effect of ambient environment on the sample imaging quality. The dashed blue box shows degradation of the material preventing from obtaining good images from the area. Thin areas are especially more prone to this degradation as

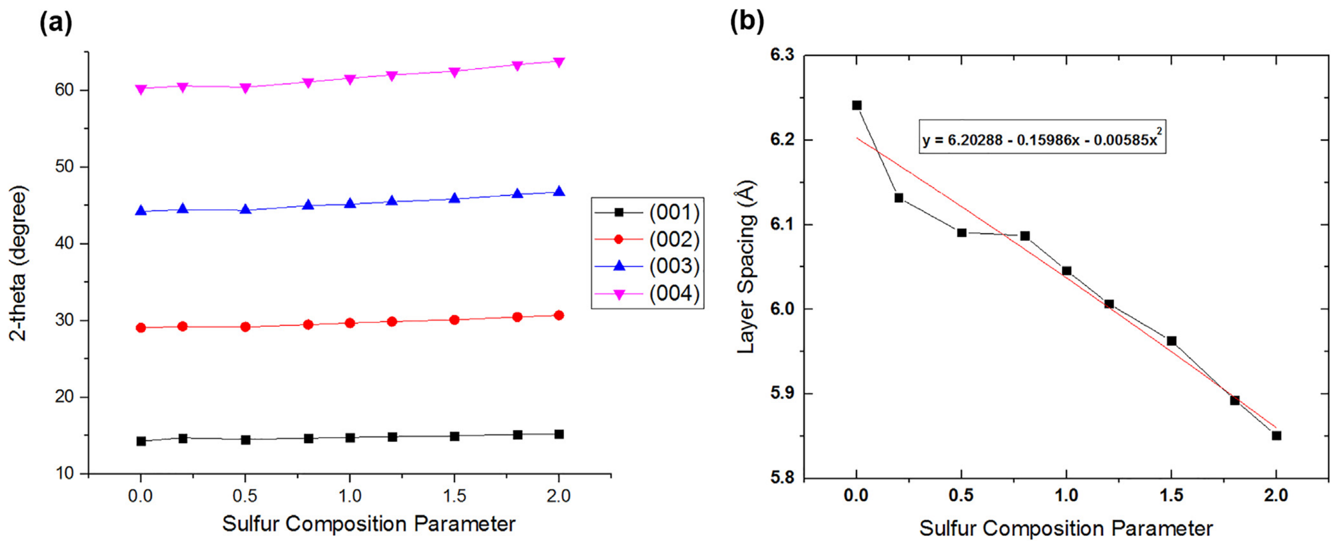

Fig. 5. (a) Graphical representation of XRD peak shifting for oriented peaks (0 0 1), (0 0 2), (0 0 3) and (0 0 4) and (b) the progression of *c*-plane spacing as a function of increasing sulfur content.

Table 3
Comparisons of *c*-axis parameter from prior experimental x-ray diffraction measurements of ZrS_xSe_{2-x} single crystals prepared by iodine vapor transport with the current study.

c-parameter (Å)	$ZrSe_2$	$ZrS_{0.5}Se_{1.5}$	$ZrS_{1.0}Se_{1.0}$	$ZrS_{1.5}Se_{0.5}$	ZrS_2
This Work	6.242	6.091	6.046	5.963	5.851
Ref. [8]	6.131	6.071	6.013	5.925	5.817
Ref. [11]	6.136	6.070	6.020	5.920	5.813

their surface to volume ratio is high. Fig. 6(e) is a zoomed in picture of Fig. 6(d) from the region inside the yellow rectangle and is utilized for plotting atomic intensity line scans to learn about stacking in the crystal. Line scan plotted along the direction of the red dashed rectangle in Fig. 6(e) is illustrated in Fig. 6(f). The intensity profile shows peaks corresponding to metal columns separated by two relatively weaker chalcogen column peaks. This is a characteristic of 1T stacking commonly observed in transition metal dichalcogenides [25]. Since the crystal is an exfoliated flake, its thickness is uncertain. But, the intensity profile in 1T stacking doesn't vary with the thickness of the crystal [26] which makes it easy to distinguish metal columns and chalcogen columns. The invariability line scan intensity profile was understood from the crystal structure models of ZrS_xSe_{2-x} alloy in top and side views, as seen in Fig. 6(g) and (h). Fig. 6(h) indicates that metal and chalcogen atoms line up on top of themselves in multilayer 1T stacking which results in the intensity profile seen in Fig. 6(f). Fig. 6(g) is a top view of

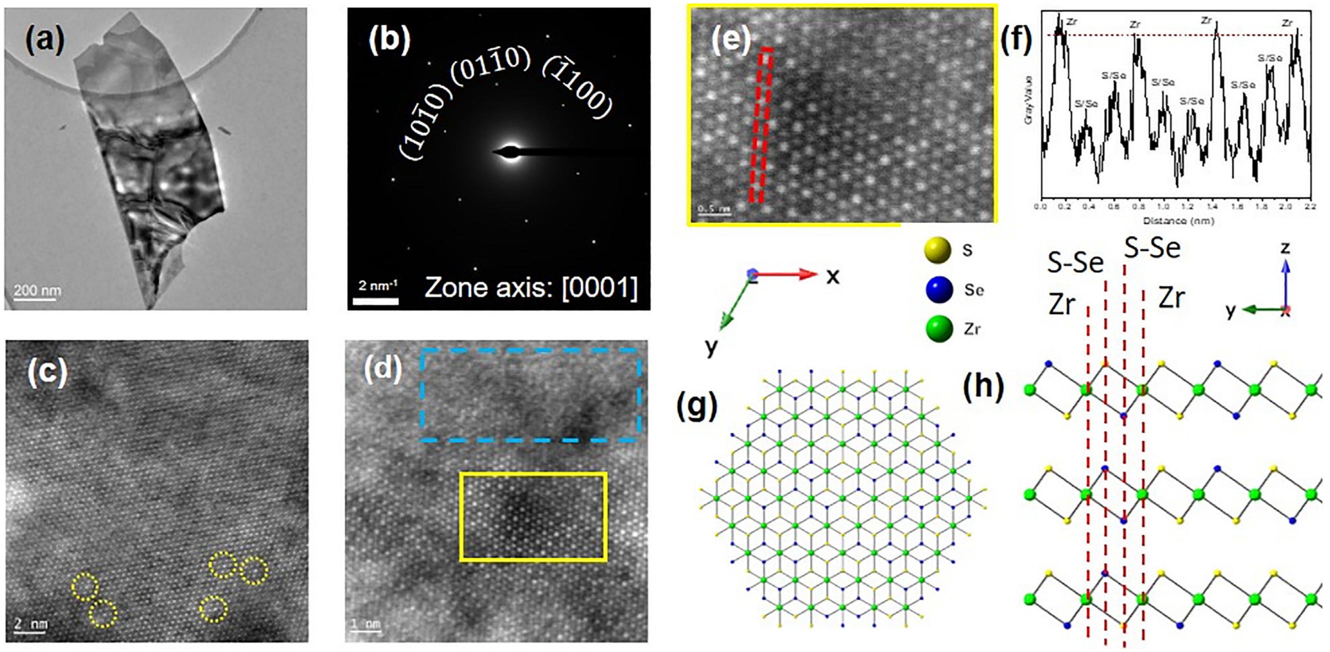

Fig. 6. (a) TEM image of an exfoliated $Zr(S_{0.5}Se_{0.5})_2$ (x = 1) alloy flake; scale bar is 200 nm, (b) SAD pattern obtained from the flake in (a); scale bar is 2 nm^{-1}, (c)–(d) atomic resolution HAADF-STEM images of $Zr(S_{0.5}Se_{0.5})_2$ (x = 1) alloy; scale bars are 2 nm and 1 nm, respectively, (e) zoomed in picture of (d) from the region outlined by yellow rectangle; scale bar is 0.5 nm, (f) Intensity profile along the line scan drawn in (e) and (g)–(h) atomic crystal structure models of $Zr(S_{0.5}Se_{0.5})_2$ (x = 1) alloy in top and side views, respectively. (For interpretation of the references to colour in this figure legend, the reader is referred to the web version of this article.)

the crystal with S (yellow) and Se (blue) chalcogens distributed in a random manner. Comparing it with Fig. 6(c) and (d), it is clear that the exfoliated flake has a uniform metal lattice with nearly equal intensities and a disordered chalcogen lattice with varying intensities. Varying intensities is an indication of variation in sulfur and selenium atom count in each chalcogen column, meaning chalcogens are distributed randomly in the lattice. This correlates well with the Raman observations indicating disorder in chalcogen lattice in the basal plane.

4. Conclusions

ZrS_2, $ZrSe_2$ and mixed alloy ZrS_xSe_{2-x} materials were synthesized through chemical vapor transport. The incongruent melting system of Zr-S-Se formed crystalline layered flakes as a transport product that grew up to 2 cm in lateral size with cm-scale flakes consistently obtained for the entire compositional range exhibiting visible hexagonal features. We have shown that the reaction products vary in stoichiometry as a function of metal source choice in terms of particle size and surface-to-volume ratio. Bulk flakes of the series ZrS_xSe_{2-x} (x = 0, 0.15, 0.3, 0.6, 1.05, 1.14, 1.51, 1.8 and 2) were analyzed through Raman spectroscopy and revealed the superposition of vibrational modes from the endpoint compounds $ZrSe_2$ and ZrS_2 together in the same spectra, but with significant asymmetrical broadening. New modes not present in the pure compounds were also found in the alloys, and most likely result from disorder-activated finite momentum phonons, enhancement of infrared modes, or from the random mixing of S and Se that introduces spatial variations in the force constants that affects lattice dynamics. Additional structural characterization was performed via x-ray diffraction (XRD) on the layered flakes to evaluate the progression of *c*-plane layer spacing function of alloy composition which was found to range between 6.24 Å for $ZrSe_2$ and 5.85 Å for ZrS_2. Estimation of the compositional ratios of the alloy flakes through energy dispersive spectroscopy (EDS) large-area mapping verified the relation of the targeted source stoichiometry represented in the layered flakes and uniform distribution of S and Se mixing in the structure. Atomic resolution HAADF-STEM imaging of the $Zr(S_{0.5}Se_{0.5})_2$ alloy validated the 1T atomic structure and enabled preliminary observation mixing in the chalcogenide lattice. Additionally, selected area diffraction pattern generated from the [0 0 0 1] zone axis reveals the in-plane lattice parameter to be approximately 3.715 Å.

Declaration of Competing Interest

The authors declare that they have no known competing financial interests or personal relationships that could have appeared to influence the work reported in this paper.

Acknowledgements

The work was financially supported by the National Science Foundation (NSF) through the Pennsylvania State University 2D Crystal Consortium – Materials Innovation Platform (2DCC-MIP) under NSF cooperative agreement DMR-1539916. Additional support provided by NSF Award No. 54-0836354 and NSF CAREER DMR-1654107.

References

[1] H.P. Vaterlaus, F. Levy, Phonons and free carriers in group IVB transition-metal dichalcogenides, J. Phys. C: Solid State Phys. 18 (11) (1985) 2351.
[2] David L. Greenaway, Rudolf Nitsche, Preparation and optical properties of group IV–VI2 chalcogenides having the CdI2 structure, J. Phys. Chem. Solids 26 (9) (1965) 1445–1458.
[3] P.A. Lee, et al., On the optical properties of some layer compounds, J. Phys. Chem. Solids 30 (12) (1969) 2719–2729.
[4] Xu-guang Zheng, Hisao Kuriyaki, Kazuyoshi Hirakawa, Electrical anisotropy of layered compound ZrSe2 and HfSe2, J. Phys. Soc. Jpn. 58 (2) (1989) 622–626.
[5] S.G. Patel, et al., Electrical properties of zirconium diselenide single crystals grown by iodine transport method, Bull. Mater. Sci. 21 (3) (1998) 213–217.
[6] Ali Hussain Reshak, Sushil Auluck, Theoretical investigation of the electronic and optical properties of ZrX2 (X= S, Se and Te), Physica B 353 (3-4) (2004) 230–237.
[7] Yan Li, Jun Kang, Jingbo Li, Indirect-to-direct band gap transition of the ZrS 2 monolayer by strain: first-principles calculations, RSC Adv. 4 (15) (2014) 7396–7401.
[8] C.R. Whitehouse, H.P.B. Rimmington, A.A. Balchin, Growth conditions and crystal structure parameters of layer compounds in the series ZrSxSe2–x, Phys. Stat. Solidi (a) 18 (2) (1973) 623–631.
[9] Mohamed Moustafa, et al., Growth and band gap determination of the ZrS x Se 2–x single crystal series, Phys. Rev. B 80 (3) (2009) 035206.
[10] S.G. Patel, S.K. Arora, M.K. Agarwal, CVT growth of zirconium sulphoselenide single crystals, Bull. Mater. Sci. 21 (4) (1998) 297–301.
[11] K.S. Bartwal, O.N. Srivastava, Growth and characterization of single crystals in the series ZrSxSe2− x, Mater. Sci. Eng., B 33 (2-3) (1995) 115–121.
[12] Hai Li, et al., Fabrication of single-and multilayer MoS_2 film-based field-effect transistors for sensing NO at room temperature, Small 8 (1) (2012) 63–67.
[13] Junhao Lin, et al., Gentle transfer method for water-and acid/alkali-sensitive 2D materials for (S) TEM study, APL Mater. 4 (11) (2016) 116108.
[14] T. Iwasaki, N. Kuroda, Y. Nishina, Anisotropy of Lattice Dynamical Properties in ZrS_2 and HfS_2, J Phys. Soc. Japan 51 (1982) 2233–2240.
[15] L.M. Xie, Two-dimensional transition metal dichalcogenide alloys: preparation, characterization and applications, Nanoscale 7 (44) (2015) 18392–18401.
[16] P. Parayanthal, Fred H. Pollak, Raman scattering in alloy semiconductors:“ spatial correlation” model, Phys. Rev. Lett. 52 (20) (1984) 1822.
[17] Sean M. Oliver, et al., The structural phases and vibrational properties of Mo1−xWxTe2 alloys, 2D Materials 4 (4) (2017) 045008.
[18] Leah Bergman, et al., Raman analysis of the configurational disorder in Al x Ga 1–x N films, Appl. Phys. Lett. 71 (15) (1997) 2157–2159.
[19] Xin Zhang, et al., Phonon and Raman scattering of two-dimensional transition metal dichalcogenides from monolayer, multilayer to bulk material, Chem. Soc. Rev. 44 (9) (2015) 2757–2785.
[20] J. Jadczak, et al., Composition dependent lattice dynamics in MoS x Se (2–x) alloys, J. Appl. Phys. 116 (19) (2014) 193505.
[21] S.M. Oliver, et al., Phonons and excitons in ZrSe2-ZrS2 alloys, J. Mater. Chem. C (2020).
[22] M.K. Agarwal, P.A. Wani, Growth conditions and crystal structure parameters of layer compounds in the series Mo1− xWxSe2, Mater. Res. Bull. 14 (6) (1979) 825–830.
[23] R.B. Murray, R.A. Bromley, A.D. Yoffe, The band structures of some transition metal dichalcogenides. II. Group IVA; octahedral coordination, J. Phys. C: Solid State Phys. 5 (7) (1972) 746.
[24] Mohamed Moustafa, et al., Angle-resolved photoemission studies of the valence bands of ZrS_xSe_{2-} x, Appl. Surf. Sci. 366 (2016) 397–403.
[25] Yung-Chang Lin, et al., Stable 1T tungsten disulfide monolayer and its junctions: growth and atomic structures, ACS Nano 12 (12) (2018) 12080–12088.
[26] Ryan J. Wu, Michael L. Odlyzko, K. Andre Mkhoyan, Determining the thickness of atomically thin MoS_2 and WS_2 in the TEM, Ultramicroscopy 147 (2014) 8–20.